Computational Condensed Matter 45 (2025) e01170

Contents lists available at ScienceDirect

Computational Condensed Matter

journal homepage: www.elsevier.com/locate/cocom

Ab initio investigation of $CaSnX_3$ (X=S and Se) chalcogenide perovskites: Structural, elastic, optoelectronic, and thermoelectric properties for photovoltaic applications

Zakarya Bouguerra [a,*], Hamza Bennacer [a,b], Abdelkader Boukortt [a], Mohamed Issam Ziane [c], Moufdi Hadjab [b]

[a] Elaboration and Physical, Mechanical, and Metallurgical Characterization of Material, Laboratory, ECP3M, Faculty of Sciences and Technology, Abdelhamid Ibn Badis University, Mostaganem, 27000, Algeria
[b] Department of Electronics, Faculty of Technology, University of M'sila, 28000, Algeria
[c] Laboratory of Electrical and Materials Engineering (LGEM), Higher School of Electrical and Energetic Engineering of Oran (ESGEEO), Oran, Algeria

ARTICLE INFO

Keywords:
Chalcogenide
Perovskite
DFT
Ab-initio
Thin film

ABSTRACT

This research paper analyzes the structural, elastic, electronic, optical, and thermoelectric properties under partial atomic substitution of the chalcogenide perovskite $CaSnX_3$ (X = S or Se) in the orthorhombic phase (Pnma, N. 62). It adopts the PBE-GGA for initial structure and energy assessments and employs TB-mBJ potential for more accurate electronic characteristics, using ab-initio DFT calculations. The study finds that substituting S with Se increases the lattice constant values while reducing the band gap, which reaches 1.27 eV when X = Se, as calculated using mBJ-GGA method. Furthermore, a new high band gap of 2.47 eV is reported for $CaSnS_3$, significantly higher than that previous research. The negative formation energy indicates that both compounds are thermodynamically and structurally stable. Elastic analysis shows they possess high stiffness, ductility, and notable anisotropy. Partial density of states analysis reveals that X_p (X = S or Se) states are related to the conduction band, while the Sn_5s/5p states are linked to the valence bands, with both compounds exhibit strong ultraviolet absorption. The thermoelectric response predicted by the BoltzTraP2 algorithm demonstrates its potential for thermoelectric and renewable energy applications.

1. Introduction

Recent advances in extensive research on materials used for harnessing renewable energies have led scientists to focus on a specific non-toxic material called perovskites. A major concern for scientists is global warming, which they aim to address by utilizing renewable energy sources and enhancing the production of materials for more efficient energy conversion[1–4]. Unlike the traditional semiconductor systems that are based on monatomic (group IV) or diatomic (III-V or II-VI) systems [5], this raises questions over these materials' capacity for performance on a scale alongside the semiconductor materials used in the first generation of solar cells and their efficiency and chemical nature. The chemical formula for these substances is typically ABX_3, where X represents an anion such as Sulfur or Selenium, B denotes a cation like Titanium or Zirconium, and cations like Calcium or Barium fill the A site [6,7]. For instance, organic and inorganic hybrid perovskite materials possess an impressive ability to absorb light, which qualifies them for usage in solar cells [8]. Additionally, the absence of lead (Pb) has a positive effect on the materials in terms of toxicity. The elements included in chalcogenide perovskites are actually less harmful than those in CIGS or CZTS, though Cu and Zn are ecotoxic in their several soluble forms [9]. The alkaline earth metals, such as calcium (Ca), serve various functions in living organisms and are not considered hazardous unless there is high exposure [10]. The presence of Sn in compounds contributes to their low toxicity, as it is naturally abundant, unlike Pb, while the chalcogen elements are nontoxic. Consequently, chalcogenide-based perovskites have significant advantages over conventional PVs, such as the newly developed lead halide perovskites, from a toxicity standpoint. In the realm of photovoltaic applications, oxide-based double perovskites have also drawn a lot of interest because of their superior light-absorption qualities and promise for extremely effective solar cells [11].

* Corresponding author.
E-mail address: zakarya.bouguerra.etu@univ-mosta.dz (Z. Bouguerra).

https://doi.org/10.1016/j.cocom.2025.e01170
Received 18 August 2025; Received in revised form 1 November 2025; Accepted 4 November 2025
Available online 5 November 2025

Table 1
Structural parameters calculated by GGA for the compounds $CaSnS_3$, and $CaSnSe_3$.

		lattice constant (Å)			B (GPa)	B'	V_0	t	ΔH_E (eV)
		A	b	C					
$CaSnS_3$	NM	6.56	6.93	10.33	63.69	4.55	3166.63	0.68	−31.81
		6.687 [24]	7.084 [24]	11.286 [24]					
		6.72 [49]	7.06 [49]	9.67 [49]					
		6.71 [101]	7.08 [101]	9.67 [101]					
$CaSnSe_3$	NM	6.92	7.34	10.87	50.53	4.60	3726.67	0.68	−12.18
	FM	6.92	7.34	10.87	50.51	4.59	3726.87		
		7.06 [101]	7.47 [101]	10.15 [101]					
$BaZrS_3$		6.91 [102]	7.03 [102]	9.84 [102]					
$BaZrSe_3$		7.23 [102]	7.28 [102]	10.29 [102]					
$ScInS_3$		6.79 [103]	9.21 [103]	6.47 [103]					
$ScInSe_3$		6.78 [103]	9.20 [103]	6.49 [103]					

Among the widely available non-toxic alternative materials, perovskite materials, particularly chalcogenides, have garnered significant attention. This interest is primarily due to their direct band gaps, high absorption, thermodynamic stability, and high conductivity [6,12–18], Several research groups have screened a variety of chalcogenide perovskite compounds of the general formula ABX_3 (where A = Ca, Sr, or Ba; B = Ti, Zr, or Hf; X = S or Se) [6,14,19–24]. Among these, several compounds have been studied experimentally, including $BaZrS_3$, Ba (Zr or Ti)S_3, $SrZrS_3$, $CaZrS_3$, and $SrTiS_3$ [16,24–26]. In addition, BaZrS3's perovskite structure has proven stable in hot, humid, and high-pressure environments [14,27]. Significant improvements in photovoltaic performance were observed in $BaZrS_3$-based solar cells, with the Ba $(Zr_{0.95}Ti_{0.05})$ S_3 model achieving an efficiency of 8.2 %, and BaZr $(S_{0.6}Se_{0.4})_3$ reaching 10.2 % by augmenting the absorber layer thickness by up to 300 nm [28]. Recent comprehensive studies on the features of chalcogenide perovskites $AHf(S, Se)_3$ (A = Ca, Sr, Ba) and their alloys, based on ab-initio calculations in the distorted orthorhombic phase, show that $CaHfSe_3$, $SrHfSe_3$, and $BaHfSe_3$ are promising candidates for solar cell applications, with optical band gaps ranging from 1.6 to 1.8 eV and high stability [29]. Studies on $AZrX_3$ (A = Ca, Sr, Ba; X = S, Se) compounds have shown that many orthorhombic β phase structures possess ideal band gaps (1.3–1.7 eV), favorable acetone binding energies, and excellent visible light absorption, making them promising options for solar cell applications [30]. $CaSnS_3$ is another promising material, featuring a wide band gap of 1.74 eV at room temperature [24]. A recent study on $CaSiS_3$ and $CaSiSe_3$ highlighted their high band gaps of 3.02 eV and 1.72 eV, respectively, alongside their excellent stability and strong absorption in the ultraviolet range [31]. Regarding chemical stability, the perovskite family with the general formula IIA-IVB-X_3 (where X = S, Se) demonstrates several advantageous properties, including distinct band gaps, effective carrier transport, and defect tolerance [18,25,26,31–33]. A recent study indicates that $BaZrS_3$ and $BaZrSe_3$ have band gaps of 1.83 eV and 1.3 eV, respectively, at the symmetry point Γ [34]. Another study on the same material using the modified Becke–Johnson (mBJ) method found that they are direct bandgap semiconductors, with calculated values of 1.77 eV for $BaZrS_3$ and 1.25 eV for $BaZrSe_3$ [35], and $CaZrX_3$, with X = S or Se, exhibits a direct band gap of 1.812 eV and 1.117 eV at the Γ point [36], also $SrZrS_3$ and $SrZrSe_3$ have been confirmed to be direct bandgap semiconductors with calculated values of 2.009 eV and 1.096 eV, respectively [37]. Other types include anti-perovskite compounds such as $SbPMg_3$, which has a solar power conversion efficiency of 15.8 % [38]. The discovery of emerging materials has led us to investigate one of the perovskites chalcogens created from alkali-earth-metals (Calcium).

In this work, we investigate the impact of substituting S^{2-} anions with Se^{2-} in $CaSnS_3$ chalcogenide materials, focusing on their structural, elastic, electronic, optical, and thermoelectric properties. These characteristics are systematically analyzed through first-principles calculations on density functional theory (DFT) [39,40]. Even though electronic structure and optical behavior have been studied using different approximations (PBE, HSE06, and G0W0), the prediction and validation of thermoelectric properties have received limited analysis of transport properties. Here, we address this gap by comprehensively examining thermoelectric properties based on the Tran-Blaha-modified Becke-Johnson (TB-mBJ) [41] using the BoltzTraP2 code [42].

The results presented here suggest that these materials could serve as promising absorber materials for optoelectronic applications. The findings on the chalcogenide materials of the IIA-IVB-X_3 (X = S, and Se) family highlighted their potential and are expected to stimulate experimental efforts in synthesizing high-bandgap $CaSnX_3$ (X = S, and Se)-based alloys for the next-generation of lead-free perovskite solar cell layers.

2. Method of calculations

For these calculations, first-principles methods are used with the FP-LAPW technique in the WIEN2k software [43]. Density functional theory (DFT), a trusted and precise approach for predicting the physical properties of various materials, is employed to evaluate the structural, elastic, electronic, and optical properties of $CaSnX_3$ (X = S and Se). The structural properties are analyzed using the Perdew-Becke-Ernzerhof method within the generalized gradient approximation (PBE-GGA) [44,45]. The resulting data were then fitted to the Murnaghan equation of state, as shown in Eq. (1) [46]. Using the IRelast program in conjunction with WIEN2k, the elastic properties were calculated precisely.

$$E(V) - E(V_0) = \frac{B_0 V}{B_0'}\left[\frac{(V_0/V)^{B_0'}}{B_0'} + 1\right] - \frac{B_0 V_0}{B_0' - 1} \quad (1)$$

The electronic structure and optical properties were predicted using the Tran-Blaha-modified Becke-Johnson (TB-mBJ), including the density of states (DOS), which defines the band structures and optical transitions. Analysis was without the spin–orbit coupling (SOC) interaction.

For the calculation, we set $K_{max} = 7/R_{MT}$, where R_{MT} is the average radius of the spherical muffin tin, which depends on the atoms selected for the compound. The value of K_{max} represents the maximum value of the vector wave K. With $l_{max} = 10$, the valence wave functions in the muffin-tin spheres are expanded. The muffin-tin radii for the Ca, Sn, S, and Se atoms were set in the range of [2.2 to 2.25 a. u]. For complete Brillouin zone sampling, 10 × 10 × 10 K-point mesh was used for sampling the irreducible wedge of the Brillouin zone, and a denser 20 × 10 × 10 × 10 K-points employed to investigate the optical properties. The ELATE model [47] was applied to analyze 2D and 3D elastic moduli, using the elastic properties obtained from WIEN2k [48]. Using the BoltzTraP2 code and applying the constant relaxing time approximation (CRTA), the thermoelectric properties were assessed across a wide range of carrier concentrations and temperatures ranging from 100 K to 900 K, considering both n-type and p-type doping.

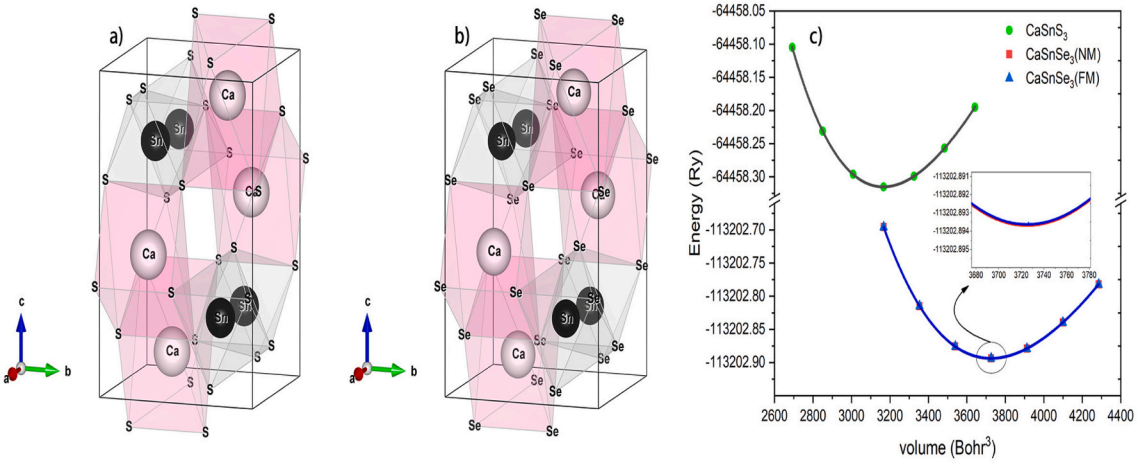

Fig. 1. Crystal structure of $CaSnS_3$ (a) and $CaSnSe_3$ (b) with the optimized volume (c) using the GGA approach.

3. Results and discussions

3.1. Structural and stability characteristics

In this section, we first examine the structural parameters, such as the lattice constant and compressibility (B) of $CaSnX_3$ (X = S or Se) compounds in their orthorhombic form with the Pnma space group (N. 62). Using the GGA approach, we calculated the structural parameters of compounds in the non-magnetic (NM) state for $CaSnS_3$ and $CaSnSe_3$, as well as in both ferromagnetic (FM) and non-magnetic (NM) configurations (see Table 1). It is evident that the proposed chalcogenide perovskites are stable in the non-magnetic (NM) state. Fig. 1 (a, b) shows the atomic positions and the conventional geometric configuration of $CaSnX_3$ (X = S and Se) compounds, using VESTA software. The graph in Fig. 1 (c) illustrates the relationship between total energy and volume, derived from calculations of the total energy of these substances using Eq. (1).

This fit procedure is employed to estimate the values of the lattice constant, compressibility modulus (B), and the first derivative ($B^{'}$) as mentioned in Table 1. It displays both the previously determined (theoretical or experimental) lattice constants and the new optimized lattice constants. GGA functionals were used to compute the structural parameters of compounds in ferromagnetic (FM) and non-magnetic (NM) configurations (see Table 1), and it was clear that the proposed chalcogenide perovskites are stable in a non-magnetic (NM) configuration.

The ground-state lattice parameters for $CaSnS_3$ were obtained by analyzing a structure similar to that in the experimental study by Shaili et al. [24]. The lattice parameters are a = 6.56 Å, b = 6.93 Å, and c = 10.33 Å, which are slightly smaller– by 1.92 %, 2.22 %, and 9.25 % respectively– compared to the experimental values along the X, Y, and Z axes. The compressibility modulus is 63.69 GPa, and the corresponding volume is 3166.63 $bohr^3$. Importantly, these values are higher than those predicted by Basera et al. [49].

Replacing the S atom with Se causes an increase in the lattice constants (a, b, and c), compressibility modulus, and volume (V_0) for $CaSnSe_3$, with values of a = 6.92 Å, b = 7.34 Å, and c = 10.87 Å, B = 50.53 GPa, and V_0 = 3726.67 $bohr^3$. Each atom has a specific R_{mt} that depends on its atomic configuration. Atoms with the highest electronic distribution exhibit a large lattice constant and volume but have lower compressibility, as shown in Table 1. These values are lower than those reported in previous studies for $CaSnSe_3$. Meanwhile, the bulk modulus (B) decreased. Structurally, as illustrated in Fig. 1, the stability of perovskites can be predicted using the ionic radii of their constituent elements, described by the tolerance factor as [50]:

Table 2
Calculated elastic and mechanical parameters utilizing the GGA approximation.

	$CaSnS_3$	$CaSnSe_3$
C_{11} (GPa)	154.71	107.98
C_{22} (GPa)	109.18	90.96
C_{33} (GPa)	105.87	85.93
C_{44} (GPa)	23.75	14.97
C_{55} (GPa)	35.17	24.53
C_{66} (GPa)	29.81	20.46
C_{12} (GPa)	35.30	26.57
C_{13} (GPa)	44.64	33.71
C_{23} (GPa)	32.37	25.94
B_H (GPa)	64.89	50.51
G_H (GPa)	33.85	24.09
E_H (GPa)	86.52	62.37
σ_H	0.28	0.29
T_D (K)	354.76 ± 300	247.38 ± 300
B_H/G_H	1.92	2.10

$$t = \frac{(R_A + R_X)}{\sqrt{2}\,(R_B + R_X)} \tag{2}$$

where R_A, R_B, and R_X are the ionic radii of A, B, and X, respectively. Experimental results and theoretical studies demonstrate that a cubic phase can form if $0.9 > t > 1.0$, if t exceeds 1.0, a hexagonal or tetragonal phase may appear, and if t is below 0.9, an orthorhombic or rhombohedral phase may occur [31,51,52]. The Goldsmith tolerance factor, calculated and presented in Table 1, indicates the structure stability, with a value of t = 0.68, which is less than 0.9. Additionally, we analyzed the formation energy of the compounds to assess how substituting sulfur with selenium affects their thermodynamic stability. For mechanical stability and successful experimental synthesis, the formation energy per atom (ΔH_E) must be negative [53]. As described in Eq. (3) [54], ΔH_E is determined where E_{Ca}, E_{Sn}, E_S, and E_{Se} denote the energies of each individual atom of a compound.

$$\Delta H_E = E_{Total} - \left(E_{Ca} + E_{Sn} + 3E_{S/Se}\right) \tag{3}$$

The negative formation energy values, listed in Table 1 as −31.81 eV ($CaSnS_3$) and −12.18 eV ($CaSnSe_3$), confirm the mechanical stability of these materials. Notably, the overall stability of the compounds is preserved, even with the formation energy value increase as a result of this substitution. Although $CaSnSe_3$ has not yet been experimentally synthesized and all previous studies are purely theoretical, its negative formation energy indicates thermodynamic stability and strongly supports the feasibility of its synthesis via various techniques, such as Ultrasonic Spray Deposition [24], Solid State Reaction [16] which proven

Table 3
The calculated band gaps of chalcogenide perovskites $CaSnS_3$ and $CaSnSe_3$. (Direct band gaps symbols with ***d***).

	PBE	HSE_{06}	G_0W_0@PBE	TB-mBJ
$CaSnS_3$	0.31_d	–	–	2.47_d
	0.76_d [49]	1.40_d [49]	1.43_d [49]	–
	0.77 [101]	1.40 [101]	1.44 [101]	–
	0.54 [24]	–	–	1.74_d [24]
$CaSnSe_3$	0.03_d	–	–	1.27_d
	0.25 [101]	0.70 [101]	0.79 [101]	–

in the field and aim to enhance PV performance.

We used the GGA optimization approach to determine the elastic properties of $CaSnX_3$ (X = S and Se) to validate the stability of these materials. Elastic constants connect a solid's mechanical strength and its controlling microscopic characteristics, including its crystal structure and interatomic connections [55]. Single-crystal elastic constants may provide significant details on the elastic modulus and its anisotropy, mechanical stability, and phase transitions [55,56]. Table 2 presents the results of the elastic and mechanical properties, which achieved the following elastic constant (C_{ij}) criteria for the orthorhombic structure [57].

$$C_{ii} > , C_{ii} + C_{jj} - 2C_{ij} > 0 \quad (4)$$

$$C_{11} + C_{22} + C_{33} + 2(C_{12} + C_{13} + C_{23}) > 0 \quad (5)$$

Table 2 summarizes the computed constants for the compounds under investigation; all are $C_{ij}>0$, confirming the criteria for mechanical stability. C_{44}, C_{55}, and C_{66} refer to the measure of resistance to shear deformations [58,59], and C_{11}, C_{22}, and C_{33} signify resistance to compressive deformations. The values illustrated in Table 2 show that resistance to shear deformations is much lower than resistance to deformations of compressional deformations with high values. Also, we observe that $C_{11}>C_{33}>C_{12}$ for the two compounds, with C_{11}, C_{33}, and C_{12} being 154.71, 105.87, and 35.30 GPa for $CaSnS_3$, and 107.98, 85.93, and 26.57 GPa for $CaSnSe_3$. This suggests that the bond strength in the (100) and (001) planes is greater than the bond strength in the (010)

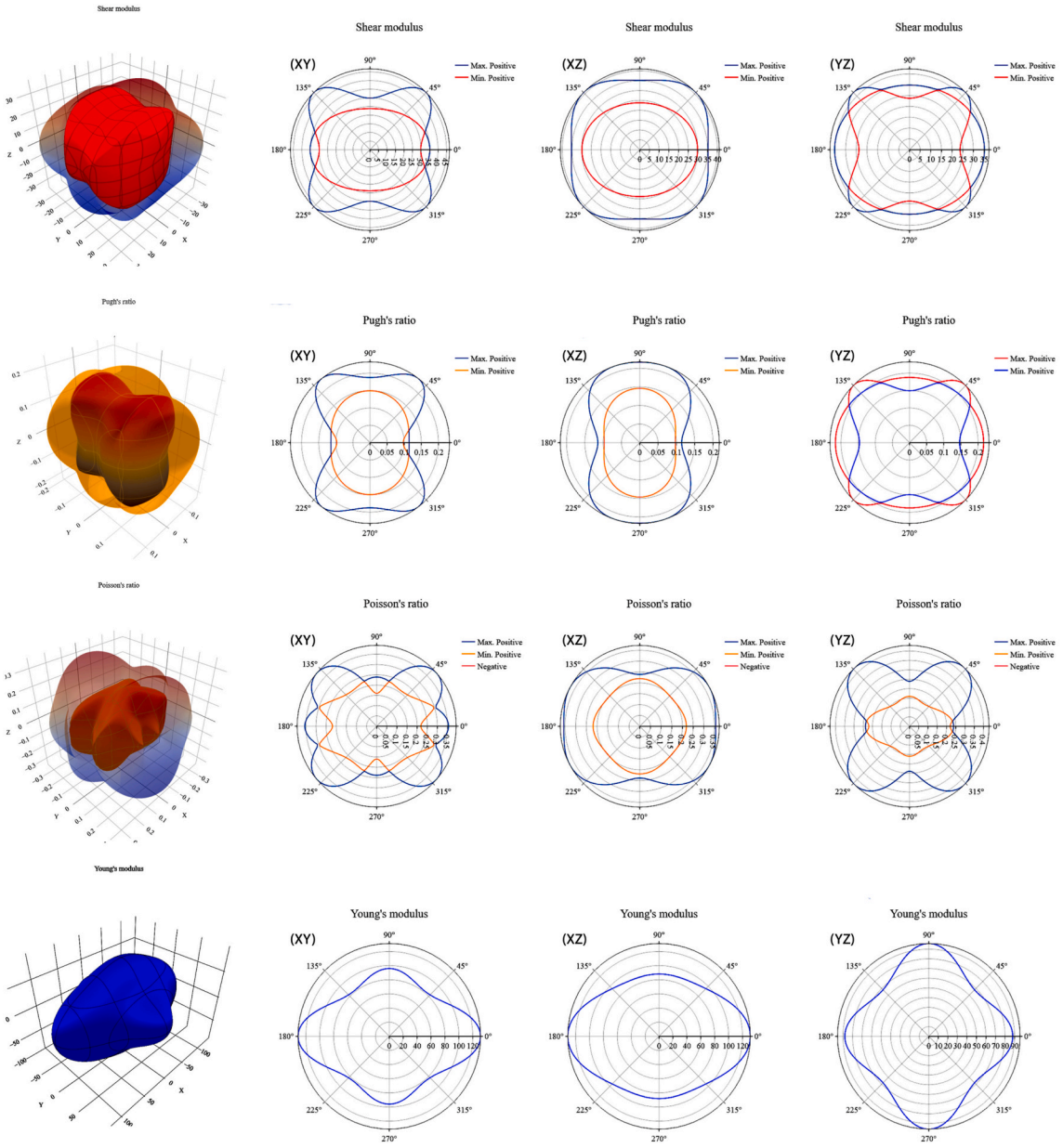

Fig. 2. The shear constant, Pugh ratio, Poisson's ratio, and Young's modulus of $CaSnS_3$ are represented in 2D and 3D.

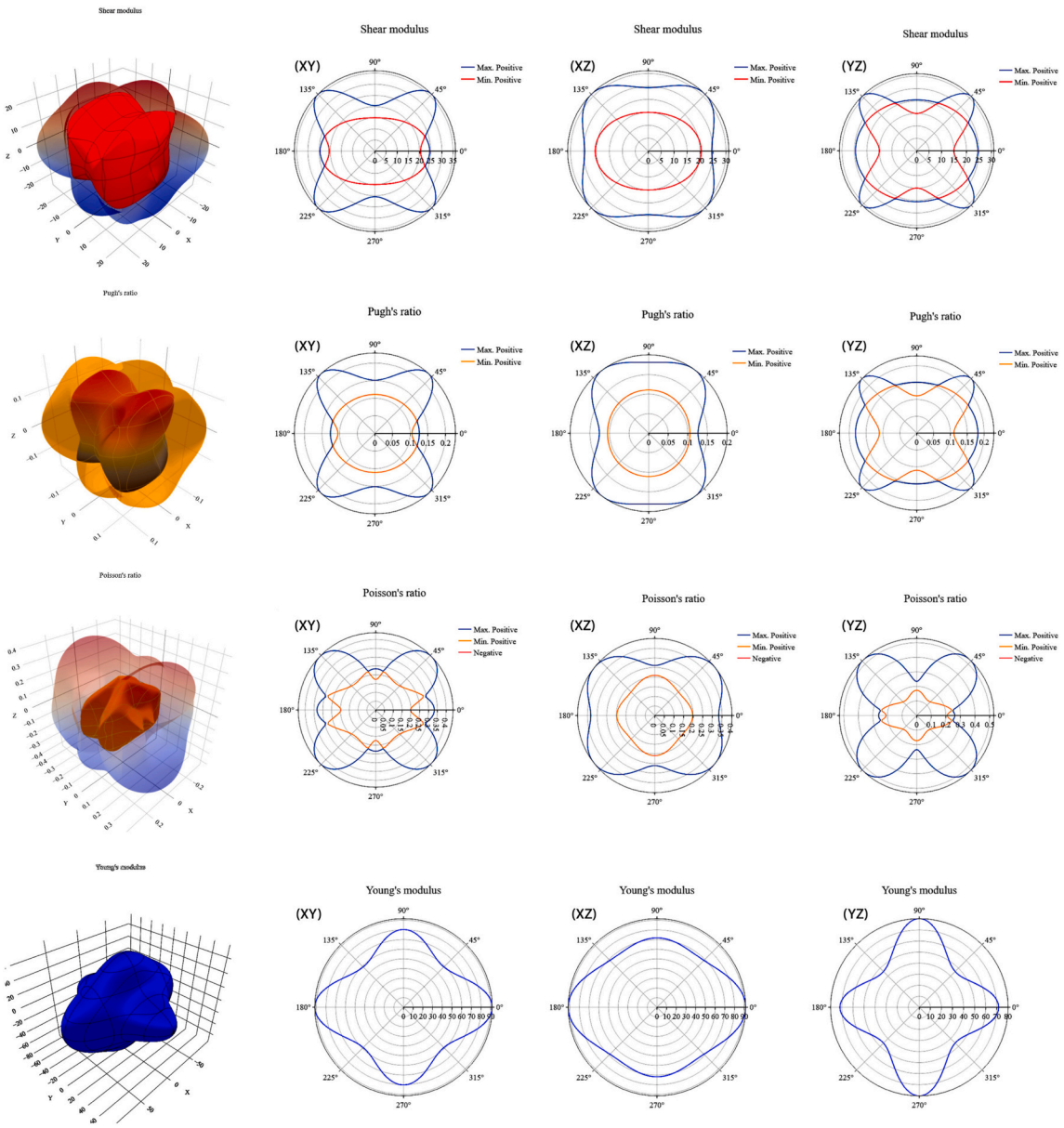

Fig. 3. The shear constant, Pugh ratio, Poisson's ratio, and Young's modulus of $CaSnSe_3$ are represented in 2D and 3D.

plane in the case of deformation according to the [100] direction.

The Pugh [60] ratio (B_H/G_H) can be used to determine if the solid compound is brittle or ductile. We can say that the solid material studied is ductile if $B_H/G_H > 1.75$. This is verified with the values listed in Table 3, which are 1.92 and 2.10 for $CaSnS_3$ and $CaSnSe_3$, respectively. The 3D surfaces and 2D projections for the shear modulus, Poisson's ratio, Pugh ratio, and Young's modulus on XY, XZ, and YZ planes are shown in Figs. 2 and 3 in a visual way. The Bulk's (B_H) and shear's (G_H) modulus ratio for an isotropic material are given by Ref. [61]:

$$B_H = (B_R + B_V)/2 \tag{6}$$

$$G_H = (G_R + G_V)/2 \tag{7}$$

The Young's modulus (E) and Poisson's ratio (σ) for an isotropic material are given with [31,62]:

$$E_H = \frac{9BG}{3B+G} \tag{8}$$

$$\sigma_H = \frac{3B-2G}{2(3B+G)} \tag{9}$$

The stiffness of the compound is measured using Young's modulus (E), with crystal anisotropy revealed by the degree of divergence from a perfect sphere in Young's moduli [63,64]. Using the ELATE module [47], elastic anisotropy and auxetic features can be analyzed, directly visualizing the 3D spherical plots and 2D projections on the XY, XZ, and YZ planes. Non-spherical contrast surfaces are observed in the calculated 3d Young's modulus using the ElATools, as evidenced in Figs. 2 and 3, which indicates the anisotropy of the examined materials.

The type of bond in a crystal can be determined by the Poisson coefficient (σ_H) [65]. Covalent, ionic, and metallic bonds are given by σ_H values of 0.1, 0.25, and 0.33, respectively. [31]. With a σ_H value of 0.28 GPa for $CaSnS_3$ and 0.29 GPa for $CaSnSe_3$, we can classify them as substances with ionic bonds. The thermal conductivity, specific heat, and lattice enthalpy are thermodynamic parameters that are connected with the Debye temperature [66,67]. The strong bonds are reflected in the high T_D value. Our estimates indicated that $CaSnS_3$ has stronger

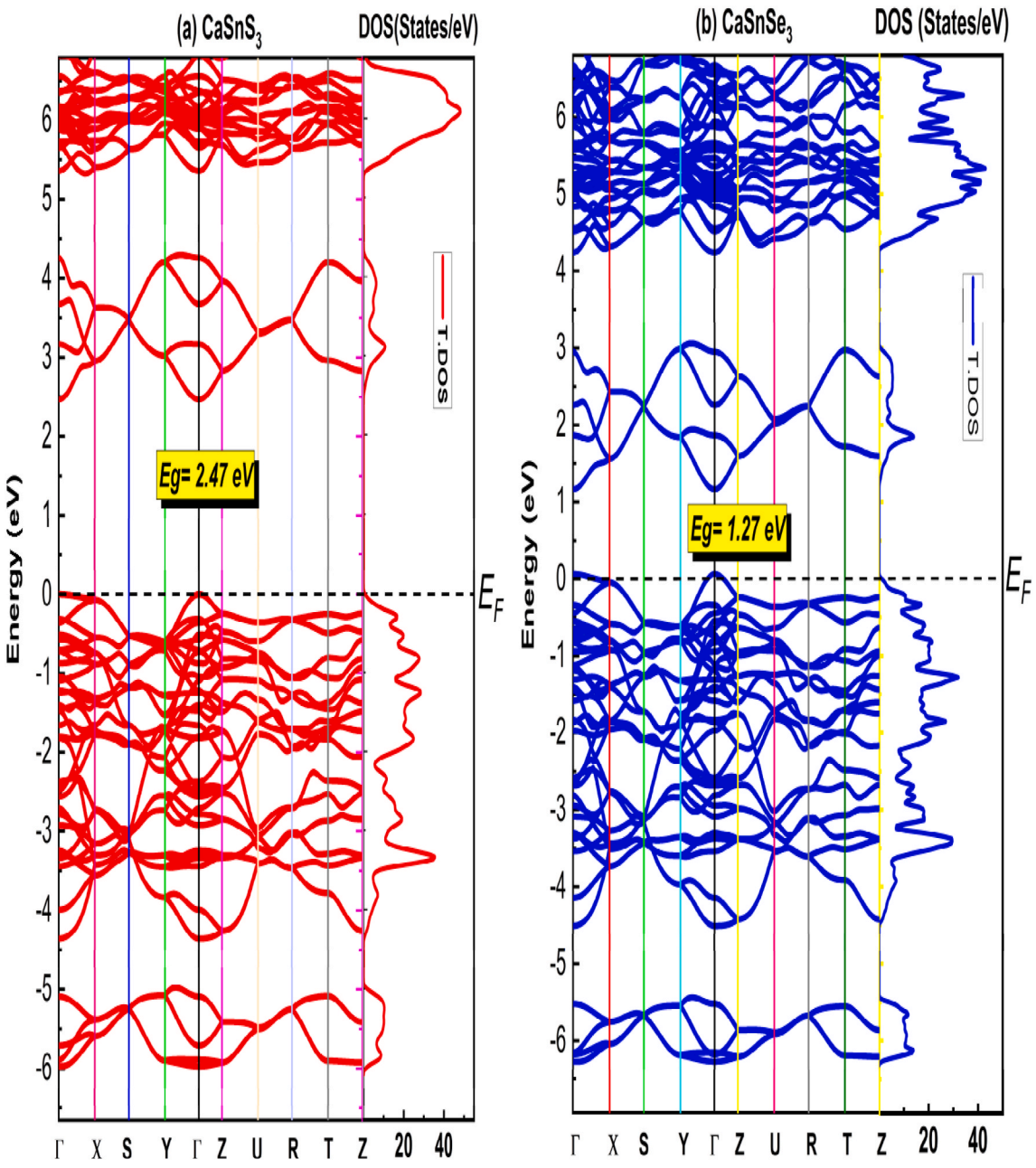

Fig. 4. Band structures of (a) $CaSnS_3$ and (b) $CaSnSe_3$ using the TB-mBJ.

bonds, with a value of 354.76 K compared to $CaSnSe_3$, which has a value of 247.38 K. We can calculate the T_D using Eq. (10) [67].

$$T_D = \frac{h}{k}\left[\frac{3n}{4\pi}\left(\frac{N_A\rho}{m}\right)\right]^{1/3} v_m \tag{10}$$

3.2. Electronic properties

Examining the band structure and density of states in this section is crucial for showcasing the solar potential, as it highlights several other properties, including thermoelectric characteristics. We have analyzed the electronic properties according to the calculated lattice parameter values for each crystal structure of $CaSnS_3$ and $CaSnSe_3$. The electronic band structures, plotted along the lines of high symmetry points within the Brillouin zone with the TB-mBJ approaches, are illustrated in Fig. 4. The two compounds $CaSnS_3$ and $CaSnSe_3$ in their stable structure, display Alloy engineering to tune the optoelectronic properties and photovoltaic performance for Hf-based chalcogenide perovskites semiconductor behaviors with a direct gap at the Γ point of the Brillouin zone, with values of 2.47 eV and 1.27 eV, respectively. It should be noted that the band dispersion for both compounds is qualitatively consistent with previous calculations for $CaSnS_3$, showing the same direct band at the Brillouin zone point (Γ). Furthermore, most dispersion curves lie in the valence and conduction bands with significant distribution, indicating that the conductivity of semiconductors remains stable despite the increase in carrier mobility. Both compounds are suitable for high-conductivity applications, such as solar cells, due to these properties. However, the range value differs, as we obtained a higher value than the experimental and theoretical studies with all previously used calculation techniques (TB-mBJ, G_0W_0@PBE, HSE_{06}, and PBE) as shown in Table 3. It should be noted that $CaSnSe_3$ has never been examined using the TB-mBJ approach, which yields valuable insights beyond prior theoretical findings.

Using the DOS, we can clarify the band structure behavior [68]. The

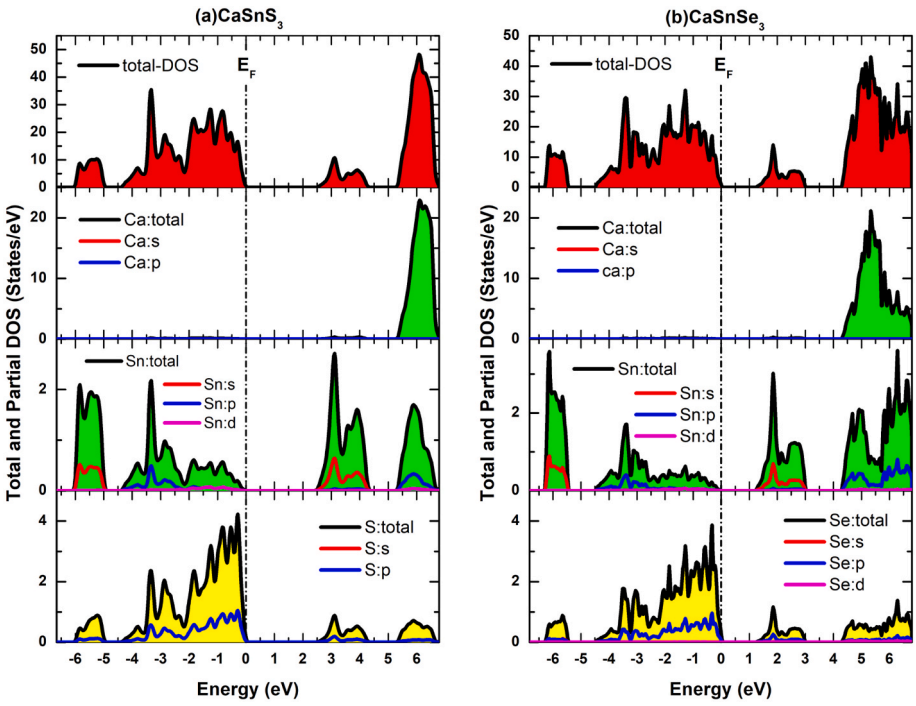

Fig. 5. TDOS and PDOS for $CaSnS_3$ (a) and $CaSnSe_3$ (b) materials using the TB-mBJ approximation.

Table 4
Zero-Frequency optical characteristics: ε_1 (0), R (0), and n (0).

	ε_1 (0)	R (0)	n (0)
$CaSnS_3$	5.71	0.12	2.08
$CaSnSe_3$	4.32	0.17	3.44

contribution of the individual atoms of the compound is evaluated by analyzing the PDOS of each atom [69]. The PDOS and TDOS for $CaSnS_3$ and $CaSnSe_3$ are sketched using the TB-mBJ approach in Fig. 5, which also confirms the semiconductor nature of these compounds due to the non-covering of the Fermi level. Density calculations were used to analyze in detail the contributions from orbitals above and below the Fermi energy level [70]. From the figure, we can see the actual role of the S_3p states for $CaSnS_3$ and the Se_4p states for $CaSnSe_3$ in forming the valence band of each compound individually, with the aid of the Sn_5s/5p states for similar trends in both compounds within the energy range of −6 to 0. The Sn_5s/5p states involved solo in the conduction band are non-overlapped at the Fermi level, making the compounds semiconductors. Replacing S^{2-} with Se^{2-} changes the influence field of Sn_5s/(2.43– 6.79 eV) to decrease to (1.22– 6.80 eV).

3.3. Optoelectronic properties

Based on the results of the TB-mBJ approach in the study of electronic properties, the presence of optoelectronic properties is confirmed using the Wien2k code within the independent-particle approximation, which neglects the excitonic (electron-hole) effects interactions. The interaction between materials and the electromagnetic wave spectrum can be fully explained by analyzing their optical properties [71,72] and determining the behavior of materials in the different visible, infrared, and ultraviolet spectral ranges. The research was simplified by studying a variety of parameters, including the dielectric constant $\varepsilon(\omega) = \varepsilon_1(\omega) + i\varepsilon_2(\omega)$, the absorption coefficient $\alpha(\omega)$, the reflectivity $R(\omega)$, and the refractive index $n(\omega)$ [73–76]. In Table 4, we mentioned the specific value of $\varepsilon_1(\omega)$, $R(\omega)$, and $n(\omega)$ at 0 eV.

The dielectric function calculated using Kramers–Kronig is stated as $\varepsilon(\omega) = \varepsilon_1(\omega) + i\varepsilon_2(\omega)$ [77]. This equation is an essential parameter in scrutinizing a material's optical characteristic behavior in electric fields, and it may be employed to estimate the other mentioned optical parameters. $\varepsilon_1(\omega)$ and $\varepsilon_2(\omega)$ are denoted as real and imaginary parts, respectively. The real part of the dielectric constant represents the phenomenon of dispersion when a photon is incident on any material [78]. Although these quantities are not independent, they follow the Kramers-Kronig relations (see Eq. (11) and Eq. (12)) [77,79,80].

$$\varepsilon_1(\omega) = 1 + \frac{2}{\pi} P \int_0^{\infty} \frac{x\varepsilon_2(x)}{x^2 - \omega^2} dx, \tag{11}$$

$$\varepsilon_2(\omega) = \frac{2\omega}{\pi} P \int_0^{\infty} \frac{\varepsilon_1(x)}{x^2 - \omega^2} dx + \frac{4\pi\sigma_{DC}}{\omega}, \tag{12}$$

The importance of the imaginary part $\varepsilon_2(\omega)$ lies in its ability to reveal the absorption characteristics and attenuation of light in the materials through the transition from the occupied states to vacant states as light traverses the medium [64,81–84]. From the analysis of Fig. 6(a and b), it was observed that $\varepsilon_1(\omega)$ and $\varepsilon_2(\omega)$ of $CaSnS_3$ and $CaSnSe_3$ started to increase from the visible zone, where they were maximal in the ultraviolet range with rising energy. At zero frequency, the values of ε_1 (0) for $CaSnS_3$ and $CaSnSe_3$ are 4.32 and 5.71, respectively. and it continues to rise until it reaches the highest value at 5.02 eV for $CaSnSe_3$, which shows a higher value than $CaSnS_3$ at 6.19 eV. The first peak of the imaginary part, referred to as the first absorption peak [85], is positioned at 3.47 eV for $CaSnS_3$ and 2.30 eV for $CaSnSe_3$, with the maximum value recorded for $CaSnS_3$ at 6.79 eV, and for $CaSnSe_3$ at 5.95 eV.

In order to evaluate the absorption field of this type of perovskite, we estimated it absorption coefficients $\alpha(\omega)$, as displayed in Fig. 6(c). Based on our findings, we can conclude that the absorption increases with rising photon energy of $CaSnX_3$ (X = S and Se). With many peaks, the first peaks of $CaSnS_3$ reach 6.28×10^4 cm^{-1} (ultraviolet), and of $CaSnSe_3$ reach 10.94×10^4 cm^{-1} (visible). They continue to reach high values in the ultraviolet range. $CaSnS_3$ has the high absorption coefficients of about 184.35×10^4 cm^{-1} compared with $CaSnSe_3$ about

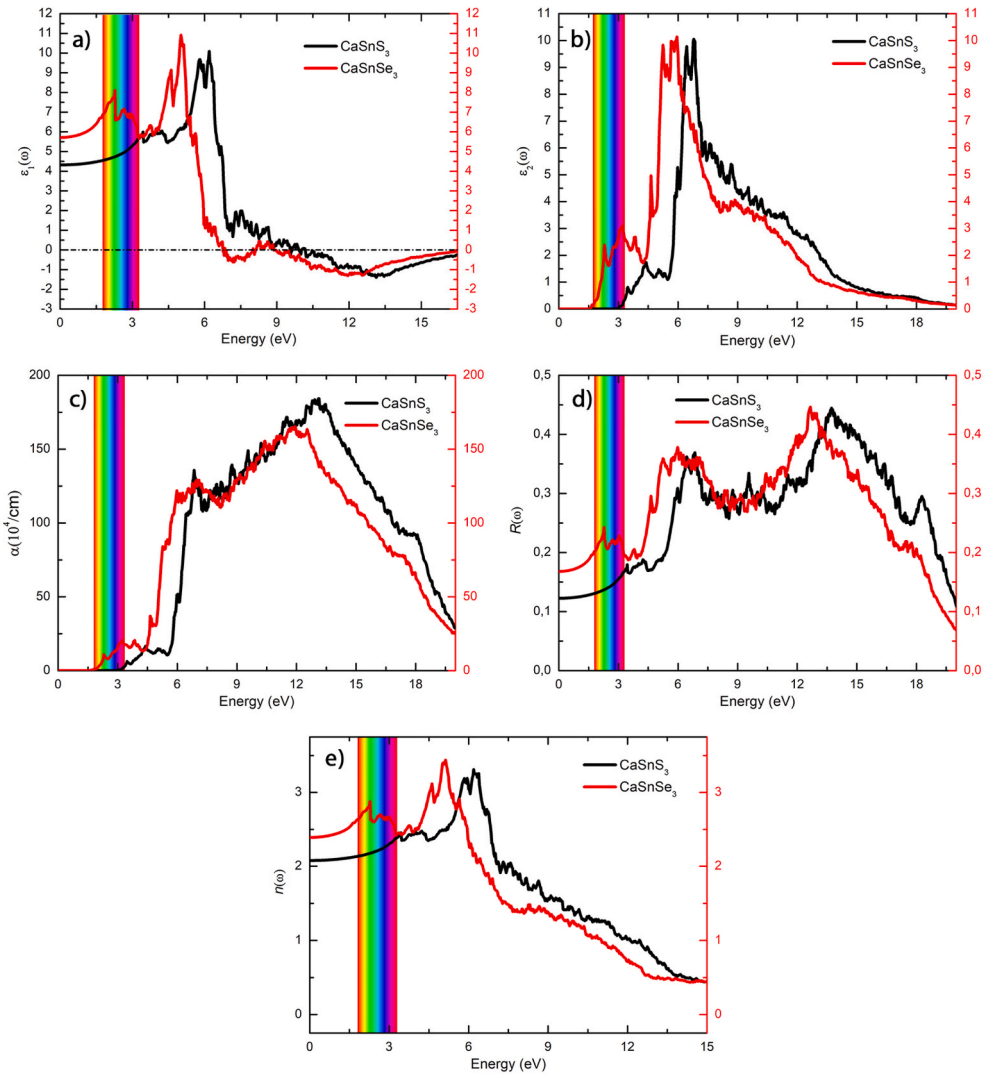

Fig. 6. (a)Real and (b)imaginary part of dielectric function, (c)absorption coefficient, (d)reflectivity, and (e)refractive index for $CaSnS_3$ and $CaSnSe_3$ calculated using the TB-mBJ.

165.36 × 10^4 cm^{-1}. Moreover, absorption in the near-infrared is not observed. The optical absorption coefficient is given with the following equation [86].

$$\alpha(\omega) = 2\omega\left[\frac{\left(\varepsilon_1^2(\omega)+\varepsilon_2^2(\omega)\right)^{1/2}-\varepsilon_1(\omega)}{2}\right]^{1/2} \tag{13}$$

Fig. 6(d) shows the reflectivity R(ω) predicted computationally, a crucial optical parameter that characterizes how well a substance reflects electromagnetic waves [78,87,88]. Notably, the static reflection coefficients R (0) calculated for both compounds are equal to ~ 0.12 for $CaSnS_3$ and 0.17 for $CaSnSe_3$. These two materials show many peaks, but with low reflectivity, they reach the same maximum value of ~ 0.44, depending on the value of the energy at 13.73 eV ($CaSnS_3$) and 12.67 eV ($CaSnSe_3$). Based on their absorption coefficients and complementary band gaps, $CaSnS_3$ (2.47 eV) is a promising candidate for use as a top cell in tandem photovoltaic structures, while $CaSnSe_3$ (1.27 eV) is well-suited both as a single-junction absorber and as a bottom cell in tandem configurations, making them valuable materials for high-efficiency photovoltaic applications.

During light transmission through a substance, the wavelength is reduced and quantified by the refractive index n(ω) that provides an explanation for how light moves within a material, specifically how its speed and direction vary when entering or exiting the medium [2,89].

The refractive index at zero frequency n (0) is known as the static refractive index and takes the root value of the real part of the dielectric function ε1 (0) given with $n(0) = \sqrt{\varepsilon_1(0)}$ [78,90]. The refractive index is plotted in Fig. 6 (e) using the TB-mBJ approach, with the n (0) values for $CaSnS_3$ and $CaSnSe_3$ reported as 2.08 and 2.39, respectively. The initial peaks of the refractive index occur at 3.44 eV for $CaSnS_3$ and 2.27 eV for $CaSnSe_3$. Subsequently, an increase in this parameter is observed, reaching its highest peak at 6.19 eV of 3.31 ($CaSnS_3$) and 5.13 eV ($CaSnSe_3$). Following that, it decreases as energy levels rise. Using the equation below, the reflectivity and refractive index of the material can be calculated by utilizing Eq. (14) and Eq. (15) [91–94].

$$\mathrm{R}(\omega) = \left[\frac{\sqrt{\varepsilon_1(\omega)+i\varepsilon_2(\omega)}-1}{\sqrt{\varepsilon_1(\omega)+i\varepsilon_2(\omega)}+1}-\varepsilon_1(\omega)\right]^2 \tag{14}$$

$$n(\omega) = \left[\frac{\varepsilon_1(\omega)}{2}+\frac{\sqrt{\varepsilon_1^2(\omega)+\varepsilon_2^2(\omega)}}{2}\right]^{1/2} \tag{15}$$

3.4. Thermoelectric properties

This study report focuses on the material's thermoelectric properties of $CaSnS_3$ and $CaSnSe_3$ at temperatures of 300 K, 500 K, 700 k, and 900

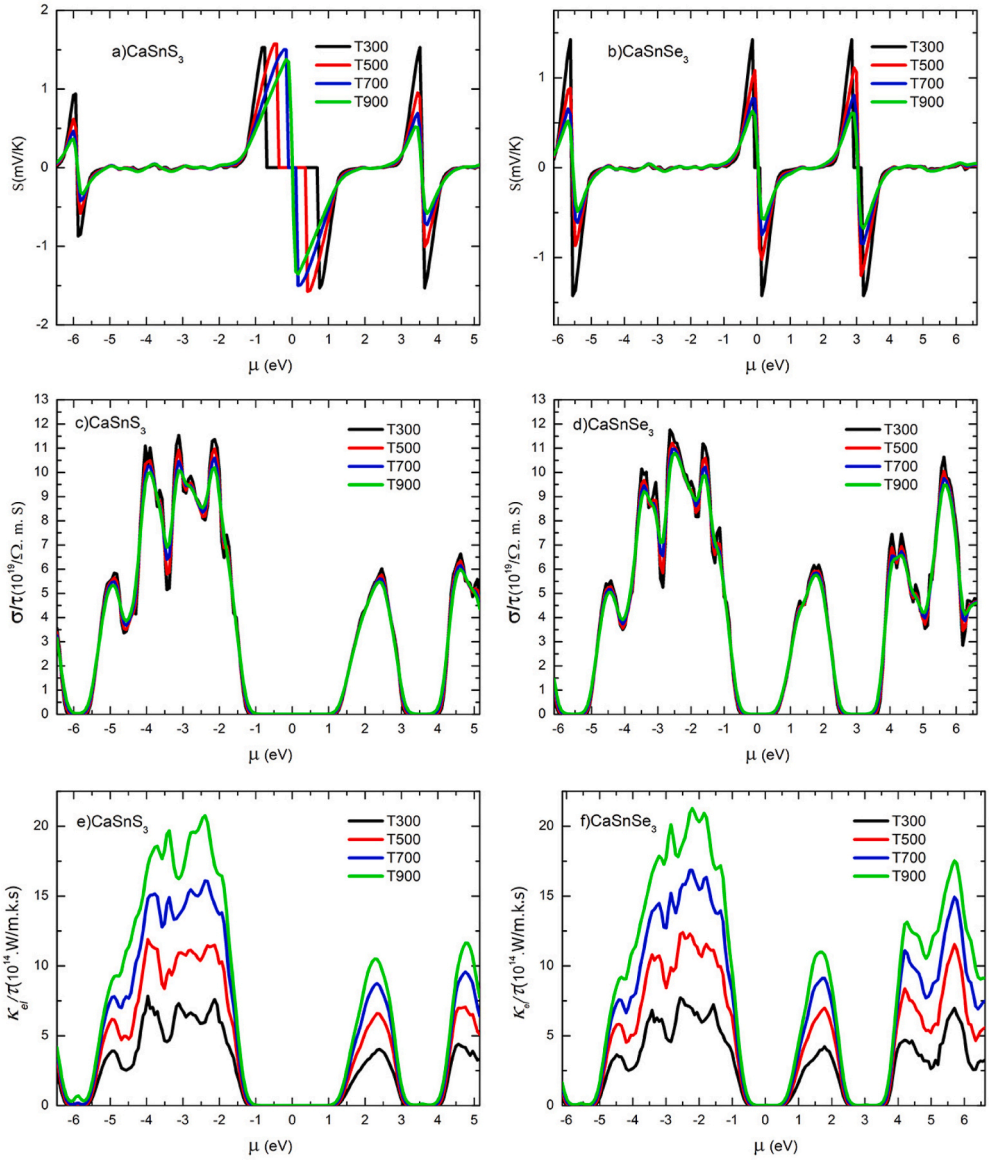

Fig. 7. The calculated Seebeck coefficient (a–b), electrical conductivity (c–d), and the electronic part of the thermal conductivity (e–f), for $CaSnS_3$ and $CaSnSe_3$.

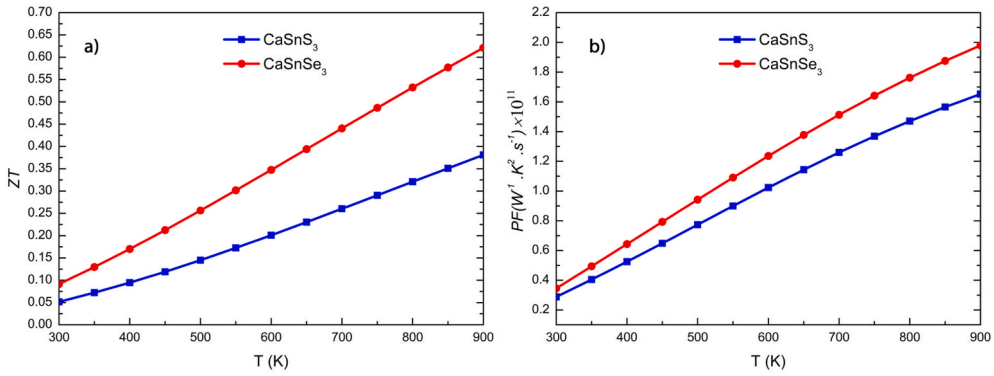

Fig. 8. Merit (a), and power factor (b) of $CaSnS_3$ and $CaSnSe_3$.

K, which are studied over a range of chemical potentials (μ) from −6.13 to 6.63 eV as shown in Fig. 7. We used the BoltzTrap2 code to investigate the Seebeck coefficient (S), electrical conductivity (σ/τ), and thermal conductivity (κ/τ), which can be evaluated using semi-classical Boltzmann transport equations [95] (see Fig. 8).

$$\sigma_{\alpha\beta}(T,\mu) = \frac{1}{\Omega}\int \sigma_{\alpha\beta}(\varepsilon)\left[-\partial f_{\mu}(T,\varepsilon)\right]d\varepsilon \tag{16}$$

$$\kappa_{\alpha\beta}(T,\mu)=\frac{1}{e^2T\Omega}\int \sigma_{\alpha\beta}\varepsilon(\varepsilon-\mu)^2\frac{\partial f_\mu(T,\varepsilon)}{d\varepsilon} \quad (17)$$

$$S=\frac{e}{T\sigma}\int \sigma_{\alpha\beta}(\varepsilon)(\varepsilon-\mu)\left[\frac{-\partial f_\mu(T,\varepsilon)}{\partial\varepsilon}\right] \quad (18)$$

With Ω, f, and μ indicating, respectively, the unit-cell volume, Fermi-Dirac distribution function, and chemical potential. The Seebeck coefficient is a tool used to measure the voltage produced by a temperature gradient [96]. The calculated Seebeck coefficient of chemical potential is shown in Fig. 7(a–b) at different temperatures for $CaSnS_3$ and $CaSnSe_3$. At room temperature, the Seebeck coefficient has a maximum value equal to 1.53 mV/K for $CaSnS_3$ and 1.42 mV/K for $CaSnSe_3$. As the value of the Seebeck coefficient shifts from the p-type with a positive value area to the n-type with a negative value zone, there is a noticeable variation in the sawtooth value of the Seebeck ratio, which decreases as temperature increases, with 1.53 mV/K at 300 K, 1.57 mV/K at 500 K, 1.50 mV/K at 700 K, and 1.38 mV/K at 900 K for $CaSnS_3$, and 1.42 mV/K at 300 K, 1.08 mV/K at 500 K, 0.77 mV/K at 700 K, and 0.63 mV/K at 900 K for $CaSnSe_3$. At 300K, the value of S swings between ±1.53 mV/K for $CaSnS_3$ and ±1.42 mV/K for $CaSnSe_3$, suggesting that most charge carriers go from electrons to holes. The anisotropic behavior can be inferred due to the differing trends in the response to a temperature difference.

Fig. 7(c and d) demonstrates that the electrical conductivity (σ/τ) disappears when the chemical potential (μ = 0) is around the Fermi level due to the absence of excited carriers. These data show that the chemical potentials (μ = 0) have no critical values for electronic conductance. The curve patterns for temperatures 300 K, 500 K, 700 K, and 900 K are the same, with each curve accompanied by a slight decrease in value. It seems that temperature has a minor influence on the electrical conductivity (σ/τ), where the p-type area exhibits larger σ/τ values than the n-type region. The connection between electrical conductivity and Seebeck values is inverse, as electrical conductivity values approach zero in regions where Seebeck values are highest. At room temperature, $CaSnS_3$ exhibits high σ/τ values of 11.53×10^{19} $(\Omega ms)^{-1}$ for p-type and 6.63×10^{19} $(\Omega ms)^{-1}$ (for n-type). For $CaSnSe_3$, the same region, the values are 11.76×10^{19} $(\Omega ms)^{-1}$ with 10.63×10^{19} $(\Omega ms)^{-1}$.

The electronic thermal conductivity per relaxation time (K/τ) for $CaSnS_3$ and $CaSnSe_3$ is shown in Fig. 7(e–f) and exhibits a similar trend to σ/τ; this observation complies with Franz-Wiedemann's law. As can be seen, the values increase with varying chemical potential from the Fermi level (μ = 0) and increasing temperature from 300 K, and the largest peak is at 900 K in the p-region with the value of 20.76×10^{14} (W/m.k.s) at −2.39 eV for $CaSnS_3$, and with a value of 21.28×10^{14} (W/m.k.s) at the chemical potential of −2.21 eV for $CaSnSe_3$. The low (K/τ) values appearing in the n-zone, with the value of 11.63×10^{14} (W/m.k.s) for $CaSnS_3$ and 17.54×10^{14} (W/m.k.s) for $CaSnSe_3$, especially at room temperature, indicate that electronic contributions to thermal conductivity are limited, making them particularly beneficial for thermoelectric applications [97].

The figure of merit for various thermoelectric materials varies, which restricts their use to applications with particular temperature ranges [98]. A thermoelectric material with a higher figure of merit, ZT, is more efficient [99]. Fig. 7 (a, b) shows that the merit ($ZT = S^2\sigma/KT$) and power factor ($PF = S^2\sigma$) rise alongside temperature. $CaSnSe_3$ shows the high values of ZT = 0.62 and $PF = 1.98 \times 10^{11}$ $(W^{-1}.k^2s^{-1})$, higher than $CaSnS_3$ (with ZT = 0.38 and $PF = 1.65 \times 10^{11}$ $(W^{-1}.k^2s^{-1})$). For comparison, $CsTaS_3$ achieves a ZT of 0.75, while $CsTaSe_3$ records a slightly lower value of 0.63 [100]. When sulfur is substituted with selenium atoms, the ZT value may be impacted by the introduction of additional charge carriers (holes).

4. Conclusion

In summary, we conducted a comprehensive study based on the density functional theory calculations about the effect of S-substitution in $CaSnS_3$ with Se on the structural, elastic, electronic, optical, and thermoelectric properties in the orthorhombic arrangement belonging to the 62_Pnma space group, using the GGA approach. This study demonstrated that the structural constants for every compound exhibit direct stability from the elastic constants and the negative formation energy values, and the ductile behavior of $CaSnS_3$ and $CaSnSe_3$ has been confirmed with Pugh's ratio values of 1.92 and 2.10, respectively. Anisotropic behavior was demonstrated by Young's modulus 3D shape design. The semiconductor nature was validated by the electronics characteristics. As a result of this substitution, the energy band gap value decreases using the TB-mBJ approach from 2.47 eV (S) to 1.27 eV (Se), and a direct band gap along with (Γ) shows a minor drop in the peak value within the absorption range, from the ultraviolet spectrum with 2.84– 13.13 eV ($CaSnS_3$) to 1.59– 11.95 eV ($CaSnSe_3$) to include the visible spectrum and exhibit very low reflectivity. The obtained band gap values indicate that $CaSnS_3$ is a promising candidate for use as a top cell in multijunction PV cells, as well as a buffer layer in thin-film solar cells for capturing high-energy photons. In contrast, the band gap of $CaSnSe_3$ is close to the theoretical optimum for a bottom cell in multijunction structures and is also suitable as a single-junction absorber. The Seebeck coefficient reveals that swapping from the p-type high-value region to the n-type low area, where $CaSnSe_3$ has a higher thermal conductivity, ZT merit, and power factor than $CaSnS_3$.

CRediT authorship contribution statement

Zakarya Bouguerra: Writing – review & editing, Writing – original draft, Visualization, Validation, Software, Methodology, Investigation, Formal analysis, Data curation. **Hamza Bennacer:** Writing – review & editing, Visualization, Validation, Supervision, Project administration, Methodology, Formal analysis. **Abdelkader Boukortt:** Writing – review & editing, Visualization, Validation, Methodology, Formal analysis. **Mohamed Issam Ziane:** Writing – review & editing, Methodology, Formal analysis. **Moufdi Hadjab:** Writing – review & editing, Methodology, Formal analysis.

Funding

No funding was received for conducting this study.

Declaration of competing interest

The authors declare that they have no known competing financial interests or personal relationships that could have appeared to influence the work reported in this paper.

Acknowledgements

The authors would like to sincerely thank everyone who helped with this Article. The Algerian DGRSDT has our sincere gratitude. This paper is part of the PRFU projects A10N01UN280120220006 and B00L02UN270120220002.

Data availability

Data will be made available on request.

References

[1] M. Tariq, M.A. Ali, A. Laref, G. Murtaza, Anion replacement effect on the physical properties of metal halide double perovskites Cs_2AgInX_6 (X=F, Cl, Br, I), Solid State Commun. (2020) 314–315, https://doi.org/10.1016/j.ssc.2020.113929.
[2] H. Murtaza, Q. Ain, J. Munir, H.M. Ghaithan, R. Sharma, A.A. Ali Ahmed, S.M. H. Qaid, A comprehensive theoretical analysis of the physical attributes of cesium-based $Cs_2LiTlCl_6$ double perovskites for eco-friendly technologies, Phys. B Condens. Matter 677 (2024), https://doi.org/10.1016/j.physb.2024.415729.

[3] S.M.H. Qaid, Q. ul Ain, H.M. Ghaithan, I. Mursaleen, A. Ahmed Ali Ahmed, J. Munir, First-principles investigations on the structural, optoelectronic, mechanical and transport properties of new stable lead-free double perovskites $Cs_2BB'I_6$ (B = Ag/Rb, B′ = Bi/Ga) halides, Mater. Sci. Eng., B 301 (2024), https://doi.org/10.1016/j.mseb.2024.117176.

[4] H. Murtaza, Q. Ain, J. Munir, H. Ullah, H.M. Ghaithan, A.A. Ali Ahmed, S.M. H. Qaid, Unveiling the mechanical, structural, thermoelectric, and optoelectronic potential of $K_2NaGaBr_6$ and K2RbTlBr6 double perovskites for sustainable technologies, Sol. Energy 273 (2024), https://doi.org/10.1016/j.solener.2024.112502.

[5] M. Ong, D.M. Guzman, Q. Campbell, I. Dabo, R.A. Jishi, $BaZrSe_3$: ab initio study of anion substitution for bandgap tuning in a chalcogenide material, J. Appl. Phys. 125 (2019), https://doi.org/10.1063/1.5097940.

[6] Y.Y. Sun, M.L. Agiorgousis, P. Zhang, S. Zhang, Chalcogenide perovskites for photovoltaics, Nano Lett. 15 (2015) 581–585, https://doi.org/10.1021/nl504046x.

[7] J.A. Márquez, M. Rusu, H. Hempel, I.Y. Ahmet, M. Kölbach, I. Simsek, L. Choubrac, G. Gurieva, R. Gunder, S. Schorr, T. Unold, $BaZrS_3$ chalcogenide perovskite thin films by H_2S sulfurization of oxide precursors, J. Phys. Chem. Lett. 12 (2021) 2148–2153, https://doi.org/10.1021/acs.jpclett.1c00177.

[8] S. Guo, C. Chen, Z. Zhang, Y. Cai, S. Wang, S. Gao, W. Chen, E. Abduryim, C. Dong, X. Guan, Y. Liu, P. Lu, Theoretical investigations of double perovskite Rb_2AgBiX_6 (X = Cl, Br, I) for solar cell and photocatalysis applications, Mater. Sci. Semicond. Process. 177 (2024), https://doi.org/10.1016/j.mssp.2024.108373.

[9] K.V. Sopiha, C. Comparotto, J.A. Márquez, J.J.S. Scragg, Chalcogenide perovskites: tantalizing prospects, challenging materials, Adv. Opt. Mater. 10 (2022), https://doi.org/10.1002/adom.202101704.

[10] S. Pors Nielsen, The biological role of strontium, Bone 35 (2004) 583–588, https://doi.org/10.1016/J.BONE.2004.04.026.

[11] J.K. Bairwa, S. Kumari, Oxide Double Perovskites: Bridging the Gap in Photovoltaic and Thermoelectric Applications, vol. 1, 2024 241004, https://doi.org/10.5281/ZENODO.15007864.

[12] W. Meng, B. Saparov, F. Hong, J. Wang, D.B. Mitzi, Y. Yan, Alloying and defect control within chalcogenide perovskites for optimized photovoltaic application, Chem. Mater. 28 (2016) 821–829, https://doi.org/10.1021/acs.chemmater.5b04213.

[13] X. Wei, H. Hui, S. Perera, A. Sheng, D.F. Watson, Y.Y. Sun, Q. Jia, S. Zhang, H. Zeng, Ti-Alloying of $BaZrS_3$ chalcogenide perovskite for photovoltaics, ACS Omega 5 (2020) 18579–18583, https://doi.org/10.1021/acsomega.0c00740.

[14] Y. Nishigaki, T. Nagai, M. Nishiwaki, T. Aizawa, M. Kozawa, K. Hanzawa, Y. Kato, H. Sai, H. Hiramatsu, H. Hosono, H. Fujiwara, Extraordinary strong band-edge absorption in distorted chalcogenide perovskites, Sol. RRL 4 (2020), https://doi.org/10.1002/solr.202070051.

[15] D. Tiwari, O.S. Hutter, G. Longo, Chalcogenide perovskites for photovoltaics: current status and prospects, JPhys Energy 3 (2021), https://doi.org/10.1088/2515-7655/abf41c.

[16] S. Niu, J. Milam-Guerrero, Y. Zhou, K. Ye, B. Zhao, B.C. Melot, J. Ravichandran, Thermal stability study of transition metal perovskite sulfides, J. Mater. Res. 33 (2018) 4135–4143, https://doi.org/10.1557/jmr.2018.419.

[17] J. Xu, Y. Fan, W. Tian, L. Ye, Y. Zhang, Y. Tian, Y. Han, Z. Shi, Enhancing the optical absorption of chalcogenide perovskite $BaZrS_3$ by optimizing the synthesis and post-processing conditions, J. Solid State Chem. 307 (2022), https://doi.org/10.1016/j.jssc.2021.122872.

[18] T. Gupta, D. Ghoshal, A. Yoshimura, S. Basu, P.K. Chow, A.S. Lakhnot, J. Pandey, J.M. Warrender, H. Efstathiadis, A. Soni, E. Osei-Agyemang, G. Balasubramanian, S. Zhang, S.F. Shi, T.M. Lu, V. Meunier, N. Koratkar, An environmentally stable and lead-free chalcogenide perovskite, Adv. Funct. Mater. 30 (2020), https://doi.org/10.1002/adfm.202001387.

[19] E. Osei-Agyemang, C. Enninful Adu, G. Balasubramanian, Doping and anisotropy–dependent electronic transport in chalcogenide Perovskite $CaZrSe_3$ for high thermoelectric efficiency, Adv. Theory Simul. 2 (2019), https://doi.org/10.1002/adts.201900060.

[20] K. Hanzawa, S. Iimura, H. Hiramatsu, H. Hosono, Materials Design of Green light-emitting Semiconductors: Perovskite-Type Sulfide Srhfs, vol. 141, 2019, pp. 5343–5349, https://doi.org/10.1021/jacs.8b13622.

[21] M. Buffiere, D.S. Dhawale, F. El-Mellouhi, Chalcogenide materials and derivatives for photovoltaic applications, Energy Technol. 7 (2019), https://doi.org/10.1002/ente.201900819.

[22] A. Swarnkar, W.J. Mir, R. Chakraborty, M. Jagadeeswararao, T. Sheikh, A. Nag, Are chalcogenide perovskites an emerging class of semiconductors for optoelectronic properties and solar cell? Chem. Mater. 31 (2019) 565–575, https://doi.org/10.1021/acs.chemmater.8b04178.

[23] Y. Peng, Q. Sun, H. Chen, W.J. Yin, Disparity of the Nature of the band gap between halide and chalcogenide single perovskites for solar cell absorbers, J. Phys. Chem. Lett. 10 (2019) 4566–4570, https://doi.org/10.1021/acs.jpclett.9b01657.

[24] H. Shaili, M. Beraich, A. El hat, M. Ouafi, E. mehdi Salmani, R. Essajai, W. Battal, M. Rouchdi, M. Taibi, N. Hassanain, A. Mzerd, Synthesis of the Sn-based $CaSnS_3$ chalcogenide perovskite thin film as a highly stable photoabsorber for optoelectronic applications, J. Alloys Compd. 851 (2021), https://doi.org/10.1016/j.jallcom.2020.156790.

[25] S. Perera, H. Hui, C. Zhao, H. Xue, F. Sun, C. Deng, N. Gross, C. Milleville, X. Xu, D.F. Watson, B. Weinstein, Y.Y. Sun, S. Zhang, H. Zeng, Chalcogenide perovskites - an emerging class of ionic semiconductors, Nano Energy 22 (2016) 129–135, https://doi.org/10.1016/j.nanoen.2016.02.020.

[26] S. Niu, H. Huyan, Y. Liu, M. Yeung, K. Ye, L. Blankemeier, T. Orvis, D. Sarkar, D. J. Singh, R. Kapadia, J. Ravichandran, Bandgap control via structural and chemical tuning of transition metal perovskite chalcogenides, Adv. Mater. 29 (2017), https://doi.org/10.1002/adma.201604733.

[27] N. Gross, Y.Y. Sun, S. Perera, H. Hui, X. Wei, S. Zhang, H. Zeng, B.A. Weinstein, Stability and band-gap tuning of the chalcogenide perovskite $BaZrS_3$ in raman and optical investigations at high pressures, Phys. Rev. Appl. 8 (2017), https://doi.org/10.1103/PhysRevApplied.8.044014.

[28] S. Karthick, S. Velumani, J. Bouclé, Chalcogenide $BaZrS_3$ perovskite solar cells: a numerical simulation and analysis using SCAPS-1D, Opt. Mater. 126 (2022), https://doi.org/10.1016/j.optmat.2022.112250.

[29] D. Liu, H. Peng, J. He, R. Sa, Alloy engineering to tune the optoelectronic properties and photovoltaic performance for Hf-based chalcogenide perovskites, Mater. Sci. Semicond. Process. 169 (2024), https://doi.org/10.1016/j.mssp.2023.107919.

[30] D. Liu, H. Zeng, H. Peng, R. Sa, Computational study of the fundamental properties of Zr-based chalcogenide perovskites for optoelectronics, Phys. Chem. Chem. Phys. 25 (2023) 13755–13765, https://doi.org/10.1039/D3CP01522J.

[31] Z. Bouguerra, H. Bennacer, A. Boukortt, A.H. Denawi, S. Meskine, Computational investigation on structural, elastic, and optoelectronic properties of low-cost perovskites $CaSiX_3$ (X=S, Se, and Te): photovoltaic application, Comput. Condens. Matt. 41 (2024), https://doi.org/10.1016/j.cocom.2024.e00983.

[32] Y. Liang, Y. Zhang, J. Xu, J. Ma, H. Jiang, X. Li, B. Zhang, X. Chen, Y. Tian, Y. Han, Z. Shi, Parametric study on controllable growth of $SrZrS_3$ thin films with good conductivity for photodetectors, Nano Res. 16 (2023) 7867–7873, https://doi.org/10.1007/s12274-023-5412-9.

[33] Z. Yang, Y. Han, Y. Liang, W. Shen, Z. Zhang, C. Fang, Q. Wang, B. Wan, L. Chen, Y. Zhang, X. Jia, Chalcogenide perovskite $BaZrS_3$ bulks for thermoelectric conversion with ultra-high carrier mobility and low thermal conductivity, Acta Mater. 276 (2024), https://doi.org/10.1016/j.actamat.2024.120156.

[34] N. Pandit, R. Singh, P.K. Kamlesh, N. Kumar, P. Sharma, S. Kumari, T. Kumar, S. Al-Qaisi, A.S. Verma, Study of chalcogenide-based metal perovskites $BaZrX_3$ (X = S and Se): DFT insight into fundamental properties for sustainable energy generation using AMPS-1D, J. Comput. Electron. 23 (2024) 1014–1028, https://doi.org/10.1007/S10825-024-02201-5/METRICS.

[35] N. Pandit, A. Dubey, T.K. Joshi, A. Shukla, U. Rani, P.K. Kamlesh, R. Gupta, T. Kumar, K. Kaur, A.S. Verma, Effect of Anion (S^{-2} & Se^{-2}) Replacement on Photovoltaic Properties in Transition Metal (Ba-Barium) Chalcogenide Perovskites, vol. 39, 2024, https://doi.org/10.1142/S0217979225500596.

[36] N. Pandit, R. Singh, T.K. Joshi, A. Shukla, P.K. Kamlesh, A. Dubey, T. Kumar, M. S. Chauhan, A.S. Verma, Investigation of a potential photovoltaic absorber based on first principles spectroscopic screening of chalcogenide perovskites: $CaZrX_3$ (X = S, Se), J. Comput. Electron. 24 (2025) 1–19, https://doi.org/10.1007/S10825-024-02245-7/METRICS.

[37] N. Pandit, R. Singh, A. Kumar, T.K. Joshi, A. Shukla, U. Rani, P.K. Kamlesh, T. Kumar, Priyanka, A.S. Verma, Physical Properties and Power Conversion Efficiency of $SrZrX_3$ (X=S and Se) Chalcogenide Perovskite Solar Cell, vol. 38, 2024, https://doi.org/10.1142/S0217984924503457.

[38] U. Rani, P.K. Kamlesh, T.K. Joshi, R. Singh, S. Sharma, R. Gupta, T. Kumar, A. S. Verma, Computational investigation of inverse perovskite $SbPX_3$ (X = Mg, Ca, and Sr) structured materials with applicability in green energy resources, Comput. Condens. Matt. 36 (2023) e00835, https://doi.org/10.1016/J.COCOM.2023.E00835.

[39] P. Hohenberg, W. Kohn, Inhomogeneous electron gas, Phys. Rev. 136 (1964) B864, https://doi.org/10.1103/PHYSREV.136.B864/FIGURE/1/THUMB.

[40] W. Kohn, L.J. Sham, Self-consistent equations including exchange and correlation effects, Phys. Rev. 140 (1965) A1133, https://doi.org/10.1103/PHYSREV.140.A1133/FIGURE/1/THUMB.

[41] F. Tran, P. Blaha, Accurate band gaps of semiconductors and insulators with a semilocal exchange-correlation potential, Phys. Rev. Lett. 102 (2009), https://doi.org/10.1103/PhysRevLett.102.226401.

[42] G.K.H. Madsen, J. Carrete, M.J. Verstraete, BoltzTraP2, a program for interpolating band structures and calculating semi-classical transport coefficients, Comput. Phys. Commun. 231 (2018) 140–145, https://doi.org/10.17632/bzb9byx8g8.1.

[43] P. Blaha, T.U. Wien, K. Schwarz, WIEN2k: an augmented plane Wave plus Local orbitals program for calculating crystal properties. https://www.researchgate.net/publication/237132866, 2001.

[44] J.P. Perdew, A. Ruzsinszky, G.I. Csonka, O.A. Vydrov, G.E. Scuseria, L. A. Constantin, X. Zhou, K. Burke, Restoring the density-gradient expansion for exchange in solids and surfaces, Phys. Rev. Lett. 100 (2008), https://doi.org/10.1103/PhysRevLett.100.136406.

[45] M. Ernzerhof, G.E. Scuseria, Assessment of the perdew-burke-ernzerhof exchange-correlation functional, J. Chem. Phys. 110 (1999) 5029–5036, https://doi.org/10.1063/1.478401.

[46] B.F.D. Murnaghan, THE COMPRESSIBILITY OF MEDIA UNDER EXTREME PRESSURES, univ. Texas public. https://www.pnas.org, 1915.

[47] S. Yalameha, Z. Nourbakhsh, D. Vashaee, ELATOOLS: a tool for analyzing anisotropic elastic properties of the 2D and 3D materials, Comput. Phys. Commun. 271 (2022), https://doi.org/10.1016/j.cpc.2021.108195.

[48] A. Jabar, L. Bahmad, S. Benyoussef, A. Jabar, L. Bahmad, S. Benyoussef, A DFT study of structural, optical, and elastic properties of the transition metal chalcogenide compounds $SrXSe_3$ (X = Ti or Zr), J. Nurs. Res. 26 (2024) 53, https://doi.org/10.1007/S11051-024-05966-9.

[49] P. Basera, S. Bhattacharya, Chalcogenide perovskites: an emerging class of semiconductors for optoelectronics. https://doi.org/10.1021/acs.jpclett.2c01337, 2022.

[50] S.A. Khandy, D.C. Gupta, Structural, elastic and thermo-electronic properties of paramagnetic perovskite $PbTaO_3$, RSC Adv. 6 (2016) 48009–48015, https://doi.org/10.1039/c6ra10468a.

[51] M. Wang, C. Zhu, H. Hu, S. Lin, L. Zhou, Z. Wang, H. Wang, T. Zhang, Y. Li, D. Yang, P. Yang, Correlation between radiation resistance and structural factors of ABO_3-type perovskites, Nucl. Instrum. Methods Phys. Res. B 536 (2023) 88–96, https://doi.org/10.1016/j.nimb.2023.01.003.

[52] N. Ramadass, ABOa-Type oxides-their structure and Properties-A bird's eye view, Mater. Sci. Eng. 36 (1978) 231–239, https://doi.org/10.1016/0025-5416(78)90076-9.

[53] X. Luan, H. Qin, F. Liu, Z. Dai, Y. Yi, Q. Li, The mechanical properties and elastic anisotropies of cubic Ni_3Al from first principles calculations, Crystals 8 (2018), https://doi.org/10.3390/cryst8080307.

[54] A. Marjaoui, M. Ait Tamerd, M. Zanouni, Semiconducting-metallic phase transition with tunable optoelectronics and mechanical properties of halide perovskites $TlGeX_3$ (X = F, Cl) under pressure, J. Mater. Sci. Mater. Electron. 34 (2023), https://doi.org/10.1007/s10854-023-11737-4.

[55] V. Ashwin, M.M. Sheik Sirajuddeen, DFT insights into the origin of d0 ferromagnetism, mechanical stability, elastic, and acoustic anisotropy in $AZrO_3$ (A= K, rb, Cs) cubic perovskites, Phys. B Condens. Matter 654 (2023), https://doi.org/10.1016/j.physb.2022.414521.

[56] Y.M. Odeh, S.M. Azar, A.Y. Al-Reyahi, A.A. Mousa, E.K. Jaradat, N. Al Aqtash, Tuning the bandgap of cubic and orthorhombic $BaZrS_3$ by substituting sulfur with selenium, AIP Adv. 13 (2023), https://doi.org/10.1063/5.0156875.

[57] Z.J. Wu, E.J. Zhao, H.P. Xiang, X.F. Hao, X.J. Liu, J. Meng, Crystal structures and elastic properties of superhard IrN_2 and IrN_3 from first principles, Phys. Rev. B Condens. Matter 76 (2007), https://doi.org/10.1103/PhysRevB.76.054115.

[58] A. Yildirim, H. Koc, E. Deligoz, First-principles study of the structural, elastic, electronic, optical, and vibrational properties of intermetallic Pd 2Ga, Chin. Phys. B 21 (2012), https://doi.org/10.1088/1674-1056/21/3/037101.

[59] A. Benmakhlouf, A. Bentabet, A. Bouhemadou, S. Maabed, R. Khenata, S. Bin-Omran, Structural, elastic, electronic and optical properties of $KAlQ_2$ (Q = Se, Te): a DFT study, Solid State Sci. 48 (2015) 72–81, https://doi.org/10.1016/j.solidstatesciences.2015.07.006.

[60] S.F. Pugh, XCII. Relations between the elastic moduli and the plastic properties of polycrystalline pure metals, London, Edinburgh Dublin Phil. Mag. J. Sci. 45 (1954) 823–843, https://doi.org/10.1080/14786440808520496.

[61] J. Liu, X. Du, X. Wang, M. Xie, J. Li, S. Zhao, Y. Zhou, Q. Zhang, J. Fang, First-Principles calculations of elasticity properties of AgW_{20} alloy, in: J Phys Conf Ser, Institute of Physics, 2023, https://doi.org/10.1088/1742-6596/2459/1/012008.

[62] P. Ravindran, L. Fast, P.A. Korzhavyi, B. Johansson, J. Wills, O. Eriksson, Density functional theory for calculation of elastic properties of orthorhombic crystals: application to $TiSi_2$, J. Appl. Phys. 84 (1998) 4891–4904, https://doi.org/10.1063/1.368733.

[63] S. Mender, M. Labidi, S. Labidi, R. Masrour, M. Ellouze, A comprehensive theoretical analysis on structural, electronic, optical, and mechanical properties of Sr_2VRuO_6 compound, Comput. Condens. Matt. 40 (2024), https://doi.org/10.1016/j.cocom.2024.e00914.

[64] X. Du, D. He, H. Mei, Y. Zhong, N. Cheng, Insights on electronic structures, elastic features and optical properties of mixed-valence double perovskites $Cs_2Au_2X_6$ (X=F, Cl, Br, I), physics letters, section A: general, Atomic and Solid State Physics 384 (2020), https://doi.org/10.1016/j.physleta.2019.126169.

[65] T. Ghellab, H. Baaziz, Z. Charifi, H. Latelli, Enhancement of thermoelectric performances in n-type RbCrZ (Z = S, Se, Te) half-metallic ferromagnetic alloys via charge carrier concentration or chemical potential, Phys. B Condens. Matter 653 (2023) 414678, https://doi.org/10.1016/j.physb.2023.414678.

[66] Z. Ye, F. Jia, S. Xu, D. Elliston, H. Su, W. Ren, First-principles study of the structural and elastic properties of orthorhombic rare-earth aluminates $RAlO_3$ (R = Sm–Lu), J. Mater. Res. (2024), https://doi.org/10.1557/s43578-023-01279-0.

[67] X. Hao, Y. Xu, Z. Wu, D. Zhou, X. Liu, J. Meng, Elastic anisotropy of OsB_2 and RuB_2 from first-principles study, J. Alloys Compd. 453 (2008) 413–417, https://doi.org/10.1016/j.jallcom.2006.11.153.

[68] J. Munir, A.R. Mat Isa, M. Yousaf, H.A.R. Aliabad, Q.U. Ain, M.A. Saeed, Electronic, magnetic and optical properties of reduced hybrid layered complex Ni(pyz)V_4O_{10} (pyz=C4H4N2) by first-principles, J. Magn. Magn Mater. 416 (2016) 241–246, https://doi.org/10.1016/j.jmmm.2016.05.004.

[69] S. Gul, Z. Ali, S. Mehmood, I. Ahmad, Electronic structure and magnetic properties of the quaternary perovskites $LnMn_3V_4O_{12}$ (ln = La, Nd and Gd), Philos. Mag. 100 (2020) 2386–2401, https://doi.org/10.1080/14786435.2020.1765263.

[70] Ç. Yamçıçıer, C. Kürkçü, Investigation of structural, electronic, elastic, vibrational, thermodynamic, and optical properties of Mg_2NiH_4 and Mg_2RuH_4 compounds used in hydrogen storage, J. Energy Storage 84 (2024), https://doi.org/10.1016/j.est.2024.110883.

[71] M. Ijaz Khan, M. Tanveer, M. Sana Ullah Sahar, S.S.A. Gillani, S.M. Junaid Zaidi, A comprehensive DFT study on the structural, electronic, elastic, and optical behaviour of $CsPbF_3$ under the effect of stress, Results Opt. 15 (2024), https://doi.org/10.1016/j.rio.2024.100667.

[72] B. Luo, X. Wang, E. Tian, H. Song, G. Li, L. Li, Electronic, dielectric and optical properties of orthorhombic lanthanum gallate perovskite, J. Alloys Compd. 708 (2017) 187–193, https://doi.org/10.1016/j.jallcom.2017.02.267.

[73] A. Ayyaz, G. Murtaza, A. Usman, H. Alkhaldi, M.Q. Shah, S. Ali, N. Sfina, M. Younas, M. Irfan, Structural, morphological, elastic, optoelectronic and thermoelectric properties of lead-free double perovskite $Na_2AgBiBr_6$ for photovoltaic applications: experimental and DFT insight, Ceram. Int. 50 (2024) 15261–15272, https://doi.org/10.1016/j.ceramint.2024.02.002.

[74] M.A. Ali, S.A. Dar, A.A. AlObaid, T.I. Al-Muhimeed, H.H. Hegazy, G. Nazir, G. Murtaza, Appealing perspectives of structural, electronic, mechanical, and thermoelectric properties of Tl_2(Se, Te)Cl_6 vacancy-ordered double perovskites, J. Phys. Chem. Solid. 159 (2021), https://doi.org/10.1016/j.jpcs.2021.110258.

[75] B. Ul Haq, S. AlFaify, R. Ahmed, A. Laref, Q. Mahmood, E. Algrafy, Optoelectronic properties of PbSe monolayers from first-principles, Appl. Surf. Sci. 525 (2020), https://doi.org/10.1016/j.apsusc.2020.146521.

[76] Q. Mahmood, T. Ghrib, A. Rached, A. Laref, M.A. Kamran, Probing of mechanical, optical and thermoelectric characteristics of double perovskites Cs_2GeCl/Br_6 by DFT method, Mater. Sci. Semicond. Process. 112 (2020), https://doi.org/10.1016/j.mssp.2020.105009.

[77] A.B. Kuzmenko, Kramers-Kronig constrained variational analysis of optical spectra, Rev. Sci. Instrum. 76 (2005) 1–9, https://doi.org/10.1063/1.1979470.

[78] S.P. Mishra, A. Varma, A.K. Kushwaha, Structural, electronic and optical properties of $CdTiX_2$ (X = N and P): a first principles density functional theory investigation, Comput. Condens. Matt. 41 (2024), https://doi.org/10.1016/j.cocom.2024.e00974.

[79] R. De, L. Kronig, On the theory of dispersion of X-rays, J. Opt. Soc. Am. 12 (1926) 547, https://doi.org/10.1364/josa.12.000547.

[80] M. Dressel, G. Gruener, G.F. Bertsch, Electrodynamics of solids: optical properties of electrons in matter, Am. J. Phys. 70 (2002) 1269–1270, https://doi.org/10.1119/1.1516200.

[81] Y. Shen, Z. Zhou, Structural, electronic, and optical properties of ferroelectric $KTa_{1/2}$ $Nb_{1/2}$ O_3 solid solutions, J. Appl. Phys. 103 (2008), https://doi.org/10.1063/1.2902433.

[82] M. Dadsetani, A. Pourghazi, Optical properties of strontium monochalcogenides from first principles, Phys. Rev. B Condens. Matter 73 (2006), https://doi.org/10.1103/PhysRevB.73.195102.

[83] S. Akhtar, A. Hussain, S. Noreen, N. Bibi, M. Bilal Tahir, J. Ur Rehman, A comparative DFT study of $MgFe_2O_4$ and $MnFe_2O_4$ spinel ferrites at various pressures to investigate the structural, mechanical, electronic, magnetic and optical properties for multifunctional applications, Comput Theor Chem 1235 (2024), https://doi.org/10.1016/j.comptc.2024.114546.

[84] I. El Heda, J. Massoudi, R. Dhahri, E. Dhahri, F. Bahri, L.H. Omari, J.F.M. L. Mariano, The effect of transition metal substitution on the structural, elastic, optical, electrical and dielectric properties of $M_{0.5}Fe_{2.5}O_4$ (M=Co and Mg) synthesized by the auto combustion method, Mater. Chem. Phys. 296 (2023), https://doi.org/10.1016/j.matchemphys.2023.127297.

[85] D.Y. Hu, X.H. Zhao, T.Y. Tang, L.M. Lu, L. Li, L.K. Gao, Y.L. Tang, Revealing structural, elastic, electronic and optical properties of potential perovskites K_2CuBiX_6 (X=Br, Cl) based on first-principles, J. Solid State Chem. 310 (2022), https://doi.org/10.1016/j.jssc.2022.123046.

[86] M. Elamin Ketfi, H. Bennacer, S.S. Essaoud, M. Issam Ziane, A. Boukortt, Computational evaluation of optoelectronic, thermodynamic and electron transport properties of $CuYZ_2$ (Z= S, Se and Te) chalcogenides semiconductors, Mater. Chem. Phys. 277 (2022), https://doi.org/10.1016/j.matchemphys.2021.125553.

[87] G. Murtaza, M. Shanawani, D. Masotti, A. Costanzo, Optimization of a 27 MHz wireless power transmitter for unknown receiver. 2020 Xxxiiird Gen. Assem. Sci. Sym. Union Radio Sci, 2020, https://doi.org/10.23919/ursigass49373.2020.9232315.

[88] H. Serai, M.I. Ziane, H. Bennacer, M. Hadjab, A.H. Denawi, M.A. Ouali, M. Ladjal, A. Boukortt, Computational investigation on the structural, electronic and optical characteristics of earth-abundant solar absorbers Cu_2BeSnX_4 (X= S, Se, Te), Optik (2024) 171794, https://doi.org/10.1016/j.ijleo.2024.171794.

[89] H. Bennacer, A. Boukortt, S. Meskine, M. Hadjab, M.I. Ziane, A. Zaoui, First principles investigation of optoelectronic properties of $ZnXP_2$ (X = Si, Ge) lattice matched with silicon for tandem solar cells applications using the mBJ exchange potential, Optik 159 (2018) 229–244, https://doi.org/10.1016/J.IJLEO.2018.01.079.

[90] M. Bendjemai, H. Bouafia, B. Sahli, A. Dorbane, Uğur, G. Uğur, S. Mokrane, Insight into the role of weak interactions on optoelectronic properties of $LiGaTe_2$-chalcopyrite under pressure effect: DFT-D3, NCI and QTAIM investigations, Phys. B Condens. Matter 599 (2020), https://doi.org/10.1016/j.physb.2020.412463.

[91] S. Meliani, S. Kouidri, H. Rached, M. EL Keurti, M. Ould Moussa, A. Ben Slimane, First-principles prediction of asymmetric electronic structures, optoelectronic features, and efficiency for Sb_2S_3, Tl_2S, $TlSbS_2$, and $TlSb_3S_5$ compounds, Solid State Commun. 357 (2022), https://doi.org/10.1016/j.ssc.2022.114973.

[92] A. Benslimane, S. Kouidri, H. Rached, M. El Keurti, S. Meliani, M. Ould Moussa, A. Benslimane, S. Kouidri, H. Rached, M. El Keurti, S. Meliani, M. Ould Moussa, Electronic structures and optical responses of Sb_2S_3, Ag_2S, $AgSbS_2$, and Ag_3SbS_3 compounds: an assessment of DFT calculations, InJPh 98 (2024) 955–966, https://doi.org/10.1007/S12648-023-02884-9.

[93] Y. Mamouni, H. Bennacer, A. Boukortt, A. Benbedra, A.H. Denawi, N. El Houda Habibes, Investigating the optoelectronic properties of Mn and Fe doped $CuAlS_2$ for intermediate band solar cell applications, Mater. Today Commun. 41 (2024) 110508, https://doi.org/10.1016/J.MTCOMM.2024.110508.

[94] M.I. Ziane, H. Bennacer, M. Mostefaoui, M. Tablaoui, M. Hadjab, A. Saim, K. Bekhedda, Anisotropic optical properties of $Cu_2ZnSn(SxSe_{1-x})_4$ solid solutions: First-principles calculations with TB-mBJ+U, Optik 243 (2021) 167490, https://doi.org/10.1016/J.IJLEO.2021.167490.

[95] B. Sid Ahmed, B. Anissa, R. Djelti, Exploring the structural, electronic, elastic, optical and thermoelectric properties of silver-based half-Heusler semiconductors

AgYTe (Y = Li, Na, and K), Mater. Sci. Semicond. Process. 183 (2024), https://doi.org/10.1016/j.mssp.2024.108772.
[96] M. Irfan, F.A. Ibrahim, M.S. Hamdy, S.A.M. Issa, H.M.H. Zakaly, First principles investigations of linear and nonlinear optical, radiation shielding and thermoelectric properties of the non-centrosymmetric Ba-based chalcogenides $Ba_2In_2X_5$ (X=S, Te), Mater. Sci. Semicond. Process. 185 (2025), https://doi.org/10.1016/j.mssp.2024.108957.
[97] F. Shirvani, Z. Razavifar, Exploration of structural, electrical, and thermoelectric properties of two-dimensional WTe_2 in three phases through ab initio investigations, Phys. B Condens. Matter 696 (2025), https://doi.org/10.1016/j.physb.2024.416609.
[98] S. Siouane, S. Jovanovic, P. Poure, A novel identification method of thermal resistances of thermoelectric modules combining electrical characterization under constant temperature and heat flow conditions, Trans Environ. Electr. Eng. 1 (2016) 44, https://doi.org/10.22149/teee.v1i4.72.
[99] S. Zhou, B.G. Sammakia, B. White, P. Borgesen, Multiscale modeling of thermoelectric generators for the optimized conversion performance, Int. J. Heat Mass Tran. 62 (2013) 435–444, https://doi.org/10.1016/j.ijheatmasstransfer.2013.03.014.
[100] L. Benahmedi, A. Besbes, R. Djelti, First-principles study of electro-structural, mechanical, optical, and thermal properties of hexagonal chalcogenide perovskites $CsTaX_3$ (X = S, Se), Phys. B Condens. Matter 714 (2025) 417452, https://doi.org/10.1016/J.PHYSB.2025.417452.
[101] S. Adhikari, S. Das, P. Johari, Tin-Based chalcogenide perovskites: a promising lead-free alternative for stable and high-performance photovoltaics. http://arxiv.org/abs/2409.16657, 2024.
[102] N. Pandit, R. Singh, P.K. Kamlesh, N. Kumar, P. Sharma, S. Kumari, T. Kumar, S. Al-Qaisi, A.S. Verma, Study of chalcogenide-based metal perovskites $BaZrX_3$ (X = S and Se): DFT insight into fundamental properties for sustainable energy generation using AMPS-1D, J. Comput. Electron. 23 (2024) 1014–1028, https://doi.org/10.1007/S10825-024-02201-5/TABLES/7.
[103] M. Naeem, N. Muhammad, G. Murtaza, H.H. Raza, H.I. Ali, First principles investigations of chalcogenides perovskites for optoelectronic applications, J. Mater. Res. 39 (2024) 2872–2888, https://doi.org/10.1557/S43578-024-01432-3/TABLES/4.